Molecular dynamic insight into octahydro-1,3,5,7-tetranitro-1,3,5,7-tetrazocine (HMX) and the nano-HMX decomposition mechanism

Mingming Zhou,†[a] Genwang Wei,†[b] Yao Zhang,[a] Dong Xiang [ID] *[a] and Caichao Ye [ID] *[bc]

Herein, we demonstrate the use of large-scale reactive molecular dynamics simulations to identify the influence of nanostructures, size effects, and temperature for the decomposition processes of octahydro-1,3,5,7-tetranitro-1,3,5,7-tetrazocine (HMX). The bulk-phase and six types of HMX nanoparticle (30–70 Å) systems were investigated at two high temperatures (2000 K and 3000 K). The evolution of the potential energy (PE) and total number of molecules (TM) of HMX crystals and their six nanoparticle systems were analyzed and addressed, and it was revealed that the nanostructure has a great accelerative effect on the thermal decomposition of HMX. The temperature distribution, initial decomposition process, and main intermediate and gas products were traced, and showed that the initial decomposition of HMX nanoparticles is triggered by the dissociation of the N–NO$_2$ bond. With the increase in temperature, the total amount of gas molecules in HMX nanoparticles rapidly increases, which shows that the high temperature can accelerate the decomposition rate for HMX nanoparticles.

1. Introduction

Octahydro-1,3,5,7-tetranitro-1,3,5,7-tetrazocine (HMX) has been widely used as an explosive and rocket propellant, and its initial chemical processes have been investigated for many years. There has been a great deal of research over the years to investigate the initial chemical processes of HMX.[1–20] There are two main factors that can affect the initial decomposition mechanism of HMX: (1) different external stimuli, and (2) the change in the explosive itself. Ge *et al.*[1,2] studied the initial decomposition mechanism of HMX dependent on the impact velocity of shockwave loading. Sharia *et al.*[3] commented on the revealed differences between solid and gas phase decomposition that proved that the crystalline field affects the bond-breaking processes in molecules, and molecular materials are strongly dependent upon the molecular environment. Defects and deformations play an important role[4,5] in initiating chemical reactions in energetic materials by facilitating their degradation, and can consist of vacancies,[6–8] crystalline

polymorphs,[9–11] dislocations,[12,13] charged particles,[14,15] and electronic excitations.[16,17a,b,18–20]

Nanoscale energetic materials can reduce the number of defects compared to conventionally sized energetic materials. The nano-structure may lead to high-shock initiation pressure[21] and less sensitivity of the energetic materials.[22–28] The combustion rate can be controlled by changing the particle size of nano-explosives.[29–33] It has been proven that nanoHNS (2,2′,4,4′,6,6′-hexanitrostilbene) and nanoTATB are more sensitive than production grade explosives under a short duration pulse.[34,35] The shock sensitivities of nano-sized HMX particle-contained samples are obviously lower due to the more regular particle surfaces. The detonation velocities of the nano-sized HMX particle-contained samples are higher, which is caused by the larger specific surface area of the nano-sized particles.[36] The apparent activation energy as well as the thermal decomposition temperature of dense spherical nano-HMX particles were markedly decreased.[37] Liu *et al.*[38] studied the adiabatic initial decomposition processes of molecular explosive HMX nanoparticles with diameters of 1.4–2.8 nm at high temperatures from 2400 to 3000 K. Zhu *et al.*[39] employed ReaxFF molecular dynamics (MD) to simulate the physico-chemical properties accompanying some transitions of HMX nanoparticles at low temperatures. While nano-HMX has been studied for more than ten years, its pyrolysis mechanism at high temperature and closer to the actual nanoscale is unclear. Therefore, it is necessary to study the mechanism of pyrolysis at high temperature with a relatively larger nanoscale.

[a]*College of Chemistry and Environmental Engineering, Yangtze University, Jingzhou, Hubei 434023, PR China. E-mail: xiangdong@yangtzeu.edu.cn*

[b]*Academy for Advanced Interdisciplinary Studies & Department of Physics, Southern University of Science and Technology, Shenzhen, Guangdong 518055, PR China. E-mail: yecc@sustech.edu.cn*

[c]*Department of Materials Science and Engineering, Guangdong Provincial Key Laboratory of Computational Science and Material Design, Southern University of Science and Technology, Shenzhen, Guangdong 518055, PR China*

† These authors contributed equally.

In this study, we demonstrate the use of large-scale reactive molecular dynamics simulations to identify the influence of nanostructures, size effects, and temperature for the initial decomposition mechanism of HMX. Herein, we simulated bulk-phase and six types of HMX nanoparticle (30–70 Å) systems at two high temperatures (2000 K and 3000 K). The initial decomposition pathways, the evolution of the small molecule products, and the evolution of the potential energy were investigated.

2. Computational details

The LAMMPS molecular dynamics simulator was employed to perform simulations with ReaxFF-lg.[40] An amorphous molecular model of nano-HMX was established with the radius of 30–70 Å. Each possible atomic pair was assigned a different bond order cutoff value to properly identify chemical species (standard values in ReaxFF C/H/O/N high-energy simulations).[41] The original C/H/O/N ReaxFF has been used for several nitro explosives[41–44] and nanoparticles[45,46] and it correctly provided the 30–70 Å radius of nano-HMX, which was constructed from the original unit cell that was experimentally determined at room temperature.[47] The initial state of the system is shown in Fig. 1, which contains 64 molecules (S_0, 1792 atoms, 30.28 × 23.89 × 23.65 Å^3), and other systems are shown in Table 1 with three-dimensional periodic boundary conditions.

First, we relaxed the nano-HMX by energy minimization with the conjugation gradient algorithm. To further relax the particles, with the canonical ensemble (NVT) and the Berendsen thermostat at 300 K, an MD simulation was performed for 10 ps. Then, we obtained the equilibrium nano-HMX crystal structure by an isothermal-isobaric (NPT) MD simulation at 0 atm and 300 K for 15 ps. Finally, the relaxed supercell was then used as the initial structure for six subsequent separate MD simulations. The relaxed supercell was heated from 300 to 2000 and 3000 K. Isothermal-isochoric MD (NVT-MD) simulations were

then performed for 220 ps with the time step of 0.1 fs. An analysis of the products was performed with a 0.3 bond-order cutoff for all atom pairs to recognize molecular species. Within the minimum bond lifetime of 25 fs, if the distance between two atoms was less than the bond distance criterion, it was determined that the two atoms form a chemical bond.[48–52] Therefore, the molecular species, bond orders, and dynamic trajectory were determined every 50 fs. These data were used to analyze the molecular species, and provided detailed information regarding the decomposition process.

The FORTRAN code FindMole[53] based on the ideas of Strachan et al.[54] was used to analyze the dynamic trajectories and calculate the chemical species and their numbers. The Getpath script was used to output net reactions and their frequencies.

3. Results and discussion

3.1. Evolution of the potential energy (PE) and total number of molecules (TM) in the HMX and nano-HMX system

Evolution of the PE and TM in the system at 2000 K and 3000 K within 220 ps is shown in Fig. 2. Initially, the curves rapidly increase and then decrease over time, indicating that energy is first absorbed and then released during decomposition. The PE curve of HMX reaches the maximum value earlier than that of
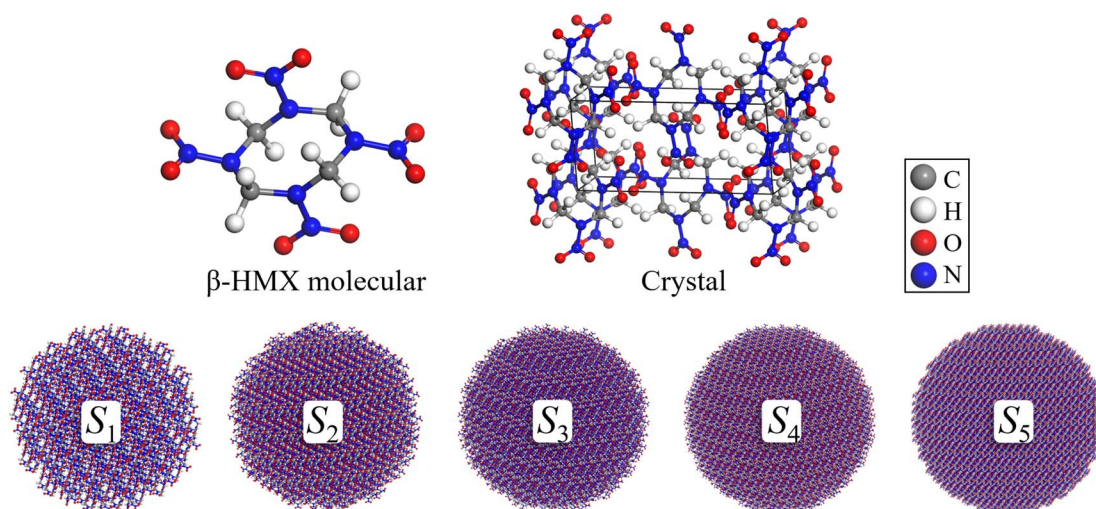
Table 1 Detailed parameters of the six HMX nanoparticle models

System	Atoms	Molecules	Radius (Å)	Length of box (Å)
S_0	1792	64	—	30.28 × 23.89 × 23.65
S_1	12 488	446	30	64 × 64 × 64
S_2	29 008	1036	40	86 × 86 × 86
S_3	56 392	2014	50	106 × 106 × 106
S_4	97 720	3490	60	126 × 126 × 126
S_5	155 288	5546	70	146 × 146 × 146

Fig. 1 Structures of a single HMX molecule, crystal HMX, and HMX nanoparticles (30–70 Å). C, H, O, and N atoms are indicated by gray, white, red, and blue, respectively. These representations also apply to the following figures.
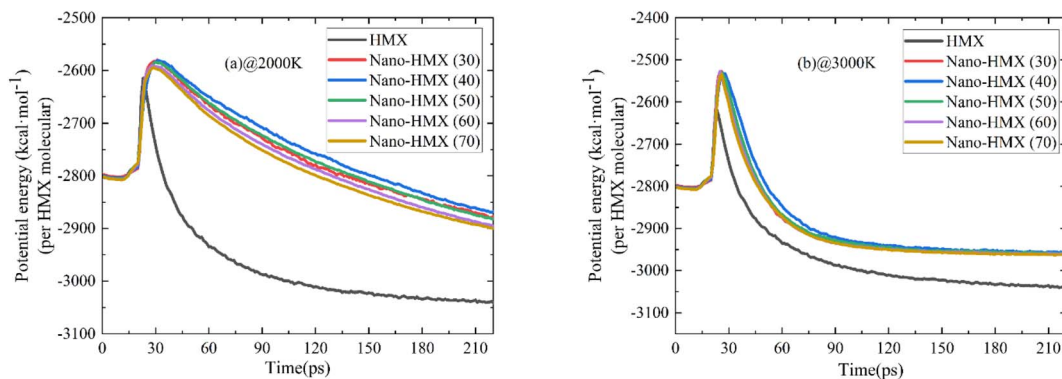
Fig. 2 Evolution of the PE of the HMX and nano-HMX system with time at (a) 2000 K and (b) 3000 K.
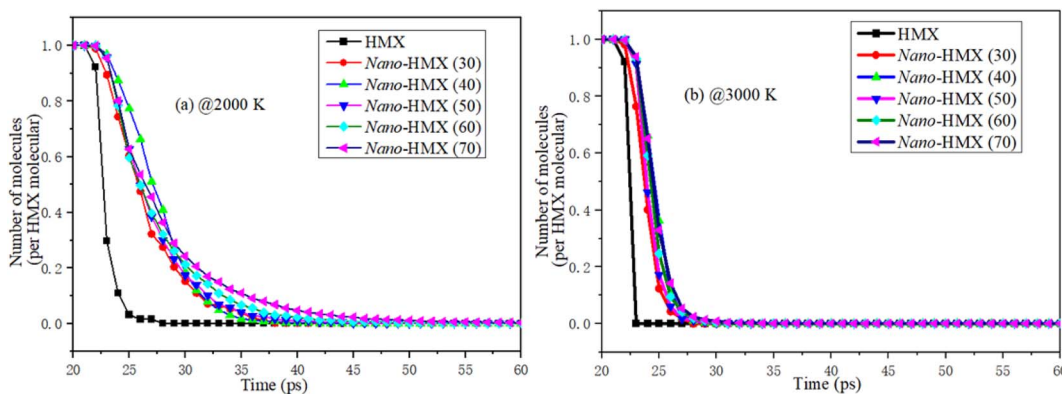

Fig. 3 Evolution of the number of HMX molecules over time at (a) 2000 K and (b) 3000 K.

nano-HMX, which indicated that it is necessary for nano-HMX to absorb more energy to achieve decomposition energy. As the temperature and nano-particle size increase, there is little change in the five PE curves. This demonstrates that the nanostructure greatly affects the PE curves, while there is little effect of nano-size and temperature on the PE curves. The PE curves of the HMX system reach stability at the maximum reaction time, which can be considered as completion of
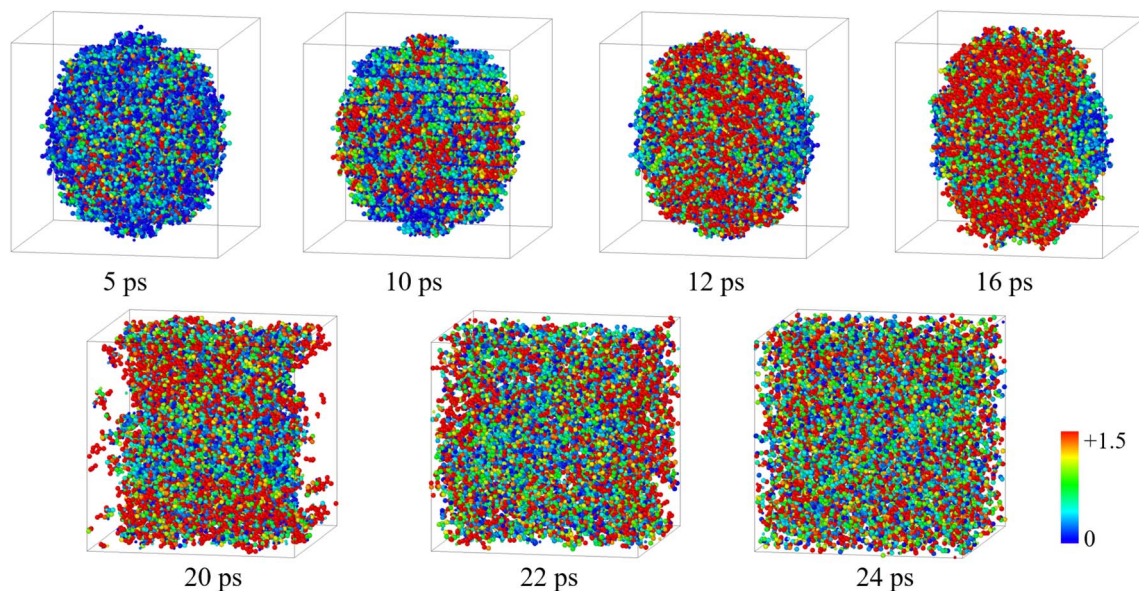

Fig. 4 Temperature distribution of 30 Å nano-HMX for 0–24 ps at 3000 K.

reaction. The PE curves of the HMX system decreased to equilibrium much more quickly as compared to the other nano-HMX system. The nano-size and temperature have little influence on the equilibrium time. There is a more rapid rate in the decrease of the PE curve, and the time to reach equilibrium is shorter for the HMX system. This indicates that the decomposition of nano-HMX is slower, and the reaction time is longer than that of the nano-HMX particles, while the nano-size and temperature have little effect on the stability of the HMX systems.

There are two turning points during the initial 30 ps of HMX thermolysis, which is interesting because the potential energy can roughly characterize the overall properties of the model system. The first turning point was at approximately 16 ps, and it may have been caused by the significant slippage in the surface layer at approximately 16 ps. This phenomenon is consistent with the conclusion in Fig. 4. The second turning point was at approximately 20 ps, and may have been caused by the rapid dispersion of the molecules and the approach of the initial decomposition reaction. At 30 ps, the maximum
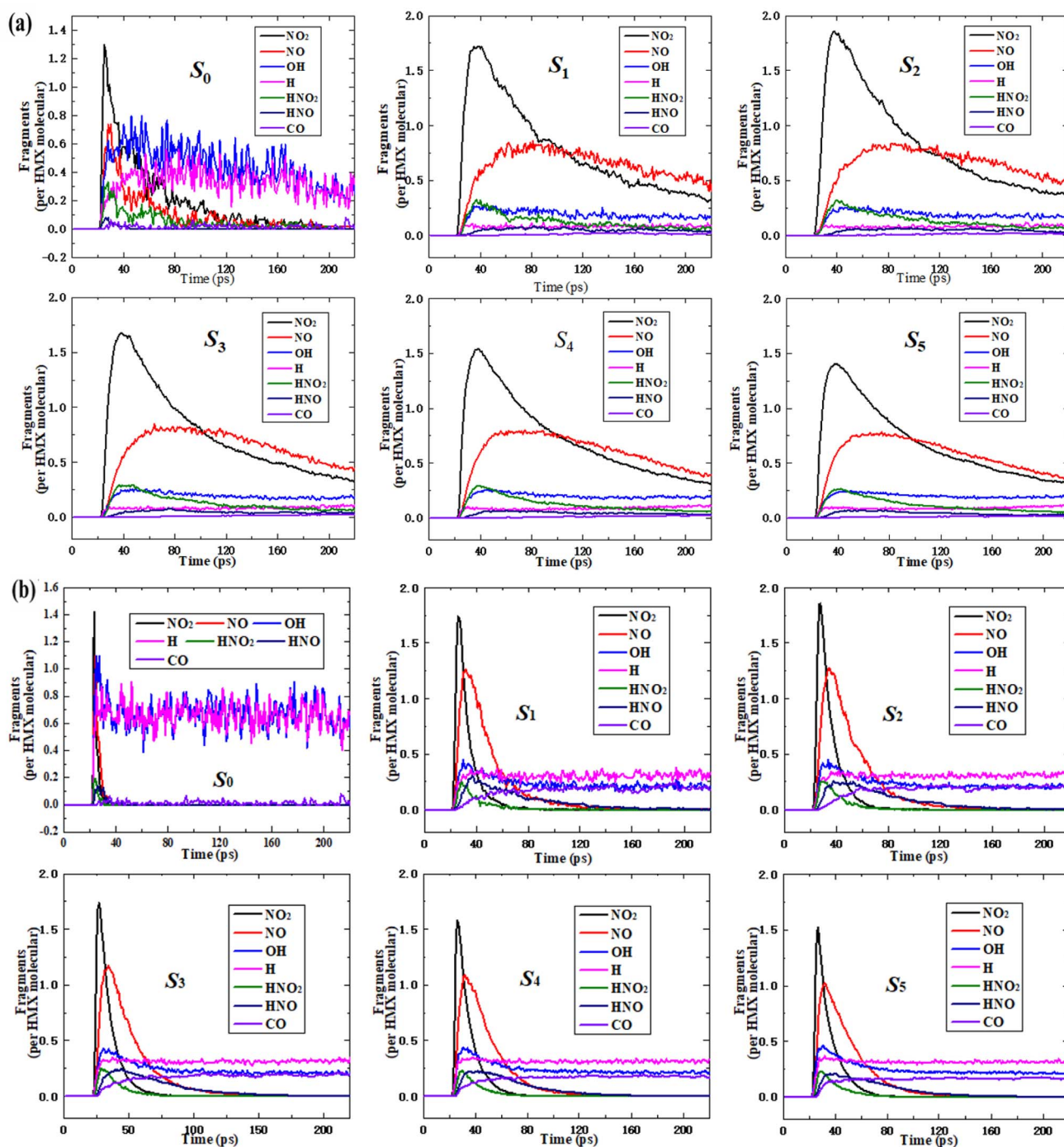

Fig. 5 The main fragment analysis of the six systems at (a) 2000 K and (b) 3000 K.

potential energy corresponded to all the nano-HMX molecules completely breaking down.

The number of molecules (NM) reflects the decomposition speed of the nano-HMX molecules. As Fig. 3 shows, the change in the NM in the system is similar at two high temperatures: first, the number of molecules remains stable for a period of the reaction time. Then, the number of molecules rapidly decreases. Finally, the number of molecules decreases during

decomposition. When the temperature is higher, there is less time to decomposition, indicating that the reactions are more violent at higher temperatures. The decomposition rate increases with the increase in the nano-size at high temperatures.

Fig. 4 shows the temperature distribution of the 30 Å nano-HMX system for 0–24 ps at 3000 K. Due to the exothermic reaction, a few hot spots emerged at 5 ps ($T > 1500$ K). The

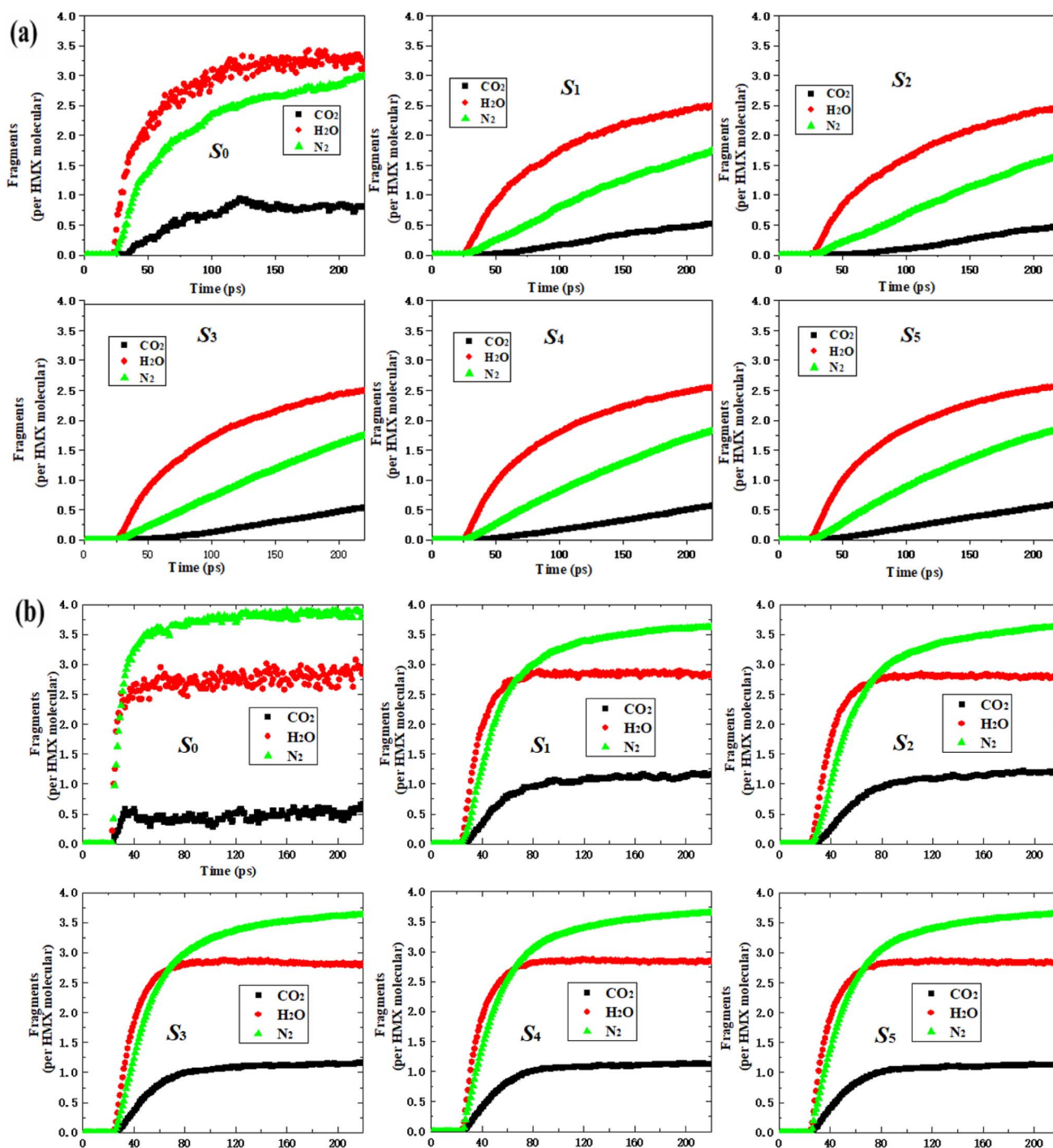**Fig. 6** Time evolution of the products CO_2, H_2O, and N_2 during the entire decomposition process of the HMX and nano-HMX systems at (a) 2000 K and (b) 3000 K. The thick trendline corresponds to the actual concentration data of the corresponding matching color.

diffusion of atoms is accelerated due to the atomic vibration conducting heat for further decomposition. The hot spots mainly occur in the center of the nano-ball (12–16 ps) and result in a microexplosion that leads to the ball falling apart (20 ps). Microexplosions promote the transfer of matter and energy to the gas phase (22–24 ps).

3.2. Decomposition reaction

The calculation results showed that the main fragments are NO_2, NO, OH, H, HNO_2, HNO, and CO in six systems at 2000 K and 3000 K, as shown in Fig. 5. All the curves of each fragment are similar for the nano-HMX system, while they are quite different from those of the HMX system. This demonstrates that the nanostructure strongly influences the main fragments. For all six systems, NO_2 fragments initially appeared, and the number of NO_2 molecules rapidly increased and then rapidly decreased. However, in the HMX system, the rate of decline was higher than that in the nano-HMX system. This demonstrates that NO_2 decreased more quickly for the HMX system than that for the nano-HMX system. The NO_2 totally decomposed for the HMX system, but for the nano-HMX system, there was less decrease in NO_2, and it tended to be in equilibrium. The NO fragment rapidly increased and then reached the maximum value faster for the HMX system than that for the nano-HMX system.

The variation trend for other nitrogenous fragments such as HNO_2 and HNO was consistent with that of the NO fragment for the six systems. All the nitrogenous fragments completely

decomposed to produce more stable products such as N_2 for the HMX system. However, they tended to be in equilibrium for the nano-HMX system, which demonstrates that the reaction for nano-HMX is much more complicated. The H fragment increased, while the H–R fragments decreased. Then, the H and OH fragments reached equilibrium. The number of OH fragments was larger than that of H fragments, which is abnormal.

To clarify the effect of temperature on the main intermediate products, an analysis was performed on the state of the major intermediate (Fig. 5(b)). The maximum of all the fragments was larger at 3000 K than that at 2000 K, while there was more rapid decomposition of all the nitrogenous fragments, which totally disappeared. This demonstrates that high temperature can accelerate the decomposition for the six systems. At 2000 K, there was little CO in the bulk HMX and nano-HMX systems. More CO was generated in the nano-HMX system than that for the bulk HMX system, which may have been caused by the nanostructure. At 3000 K, the amount of CO for the bulk HMX and nano-HMX systems increased, which may have occurred because heat increases the intensity of the pyrolysis reaction.

All the curves for CO_2, H_2O, and N_2 of each fragment are similar to those of the nano-HMX system. However, they are quite different as compared to those for the HMX system. This demonstrates that the nanostructure strongly influences the main products. For the HMX system, the curves for CO_2 and H_2O initially increased, and then reached equilibrium. The curve for N_2 rapidly increased, then slowly increased, and finally

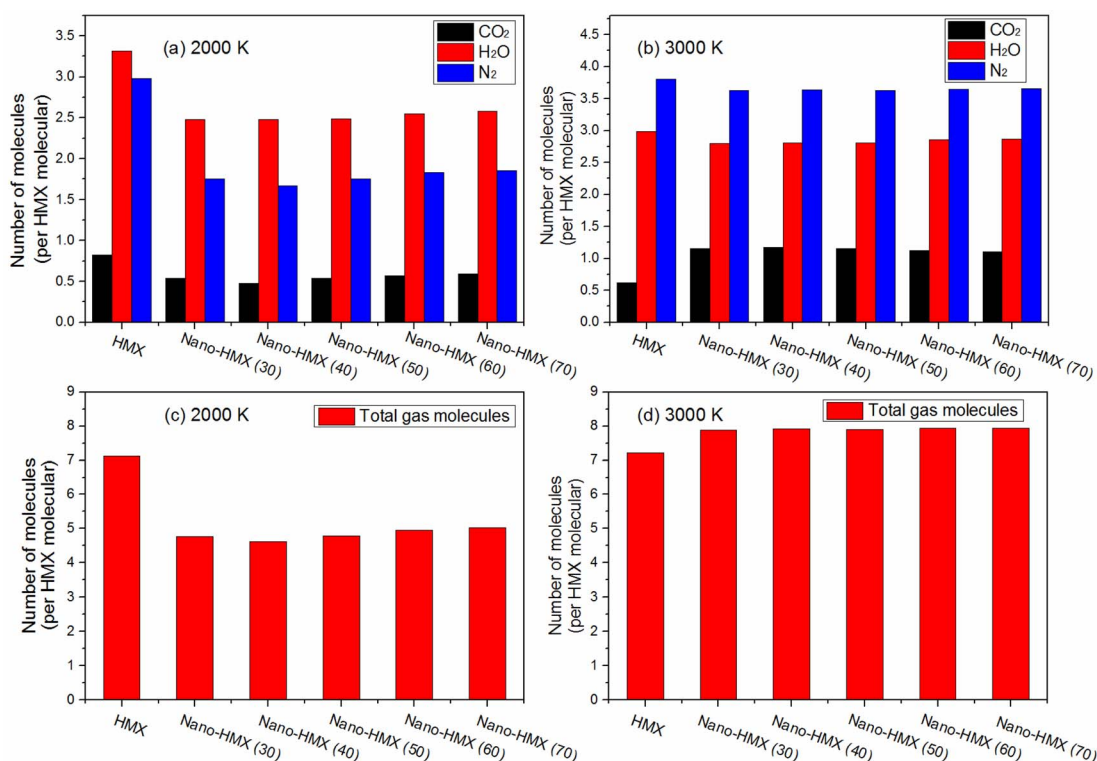**Fig. 7** Time evolution of the products CO_2, H_2O, and N_2 per HMX molecule during the entire decomposition process in the HMX and nano-HMX systems at (a) 2000 K and (b) 3000 K. Time evolution of the total gas molecules during the entire decomposition process in the HMX and nano-HMX systems at (c) 2000 K and (d) 3000 K.

Table 2 Primary reactions with the highest frequencies and the importance of 30 Å nano-HMX at 3000 K

No.	The initial reaction	Occurrence time (ps)	Frequency
R0	$C_4H_8O_8N_8 \rightarrow C_4H_8O_2N_5 + 3NO_2$	0.2	23
R1	$C_4H_8O_8N_8 \rightarrow C_4H_8O_4N_6 + 2NO_2$	0.2	17
R2	$C_4H_8O_8N_8 \rightarrow C_4H_8N_4 + 4NO_2$	0.2	12
R3	$C_4H_8O_8N_8 \rightarrow C_4H_7O_2N_5 + NO_2H + 2NO_2$	0.2	8
R4	$C_4H_8O_8N_8 \rightarrow C_4H_7N_4 + NO_2H + 3NO_2$	0.2	7
R5	$C_4H_8O_8N_8 \rightarrow C_4H_8O_6N_7 + NO_2$	0.2	2
R6	$C_4H_8O_8N_8 \rightarrow C_4H_7ON_5 + OH + 3NO_2$	0.2	2
R7	$C_4H_8O_8N_8 \rightarrow C_4H_7O_4N_6 + NO_2H + NO_2$	0.2	2
R8	$2C_4H_8O_8N_8 \rightarrow C_4H_7O_2N_5 + C_4H_8O_2N_5 + NO_2H + 5NO_2$	0.2	2

increased with rapidity once more. For the nano-HMX system, the curve for H_2O increased, and then, there was a tendency to reach equilibrium. The curves for N_2 and CO_2 monotonically increased. For the six systems, the trend of the curve height is in the following order: $H_2O > N_2 > CO_2$.

To understand the effect of temperature on the main products, the main gas products were analyzed (Fig. 6(b)). The curves for three gas products indicate that less time is required to achieve a maximum value at 3000 K than that at 2000 K. For the six systems, the curves for three gas products initially increased, and then reached equilibrium. The equilibrium value of N_2 was larger than that of H_2O, while the equilibrium value of H_2O was

larger than that of CO_2. The variation tendency for nano-HMX was similar, but the tendency for variation in the nano-HMX and HMX systems greatly differed. The increased rate of H_2O production, the main product of nano-HMX, was much higher than that of N_2 and CO_2. Nevertheless, the trends for the growth rates of H_2O and N_2 were very similar.

As the temperature increased, the amount of CO_2 and N_2 increased, while the amount of H_2O slightly decreased per HMX molecule for the nano-HMX system. However, as the temperature increased, CO_2 and H_2O decreased, while N_2 increased per HMX molecule for the HMX system. The total gas molecules were almost the same at two high temperatures for the HMX

Table 3 Elementary reactions and net flux (NF) of 30 Å nano-HMX at 3000 K

No.	Reactions	NF	No.	Reactions	NF
R0	$CO_2N_2 \rightarrow CO_2 + N_2$	5321	R31	$CN_3 + N_2 \rightarrow CN_5$	762
R1	$CO_2 + N_2 \rightarrow CO_2N_2$	5276	R32	$CO + ON \rightarrow CO_2N$	757
R2	$CON_2 \rightarrow CO + N_2$	3527	R33	$CHON_3 \rightarrow CHON + N_2$	684
R3	$CO + N_2 \rightarrow CON_2$	3477	R34	$CHON + N_2 \rightarrow CHON_3$	669
R4	$ON + N_2 \rightarrow ON_3$	3214	R35	$ON + HON \rightarrow ON + HON$	664
R5	$ON_3 \rightarrow ON + N_2$	3206	R36	$HO + ON \rightarrow HO_2N$	659
R6	$N_4 \rightarrow 2N_2$	2953	R37	$CO_2N \rightarrow CO + ON$	629
R7	$2N_2 \rightarrow N_4$	2933	R38	$H_2O_2N \rightarrow ON + H_2O$	563
R8	$CON + N_2 \rightarrow CON_3$	2623	R39	$CHN_2 + N_2 \rightarrow CHN_4$	563
R9	$CON_3 \rightarrow CON + N_2$	2620	R40	$CHN_4 \rightarrow CHN_2 + N_2$	554
R10	$2ON \rightarrow O_2N_2$	1493	R41	$HN_2 + N_2 \rightarrow HN_4$	545
R11	$HN_2 + N_2 \rightarrow HN_2 + N_2$	1443	R42	$HN_4 \rightarrow HN_2 + N_2$	537
R12	$O_2N_2 \rightarrow 2ON$	1399	R43	$ON + H_2O \rightarrow H_2O_2N$	534
R13	$H_2ON_2 \rightarrow H_2O + N_2$	1155	R44	$HO + HON \rightarrow ON + H_2O$	525
R14	$H_2O + N_2 \rightarrow H_2ON_2$	1154	R45	$C_2N_3 + N_2 \rightarrow C_2N_5$	503
R15	$HO + N_2 \rightarrow HON_2$	1126	R46	$ON + H_2O \rightarrow HO + HON$	497
R16	$ON + CON \rightarrow CO_2N_2$	1119	R47	$C_2N_5 \rightarrow C_2N_3 + N_2$	490
R17	$HON_2 \rightarrow HO + N_2$	1075	R48	$HO + H_2O \rightarrow HO + H_2O$	477
R18	$C_2O_2N \rightarrow CO + CON$	1074	R49	$H_2N_3 \rightarrow H_2N + N_2$	469
R19	$CO_3N \rightarrow CO_2 + ON$	1066	R50	$H_2N + N_2 \rightarrow H_2N_3$	456
R20	$CO_2N_2 \rightarrow ON + CON$	1050	R51	$H + N_2 \rightarrow HN_2$	395
R21	$CO + CON \rightarrow C_2O_2N$	1013	R52	$HN_2 \rightarrow H + N_2$	394
R22	$CO_2 + ON \rightarrow CO_3N$	1010	R53	$CHO_2N_2 \rightarrow CHON + ON$	386
R23	$ON + HON \rightarrow HO_2N_2$	937	R54	$H_2N_2 \rightarrow H_2 + N_2$	384
R24	$HO_2N_2 \rightarrow ON + HON$	927	R55	$CHON + ON \rightarrow CHO_2N_2$	380
R25	$C_2O_3 \rightarrow CO + CO_2$	854	R56	$C_2ON_4 \rightarrow C_2ON_2 + N_2$	378
R26	$CO + CO_2 \rightarrow C_2O_3$	844	R57	$C_2ON_2 + N_2 \rightarrow C_2ON_4$	367
R27	$HON_3 \rightarrow HON + N_2$	841	R58	$CN_3 \rightarrow CN + N_2$	361
R28	$HON + N_2 \rightarrow HON_3$	822	R59	$H_2 + N_2 \rightarrow H_2N_2$	352
R29	$HO_2N \rightarrow HO + ON$	786	R60	$CHO_2N_2 \rightarrow HN_2 + CO_2$	351
R30	$CN_5 \rightarrow CN_3 + N_2$	767	R61	$C_2ON_4 \rightarrow C_2N_3 + ON$	349

system. However, the total gas molecules rapidly increased for the nano-HMX system as the temperature increased. These results indicate that high temperature can increase the specific impulse of the nano-HMX system, which further indicates that nano-HMX may be used as a propellant (Fig. 7).

The initial decomposition paths of the six HMX systems were analyzed by a MATLAB script. Table 2 shows the most frequent and important primary reactions of 30 Å nano-HMX at 3000 K. As shown in Table 2, at 0.2 ps, the $C_4H_8O_8N_8 \rightarrow C_4H_8O_2N_5 + 3NO_2$ reaction occurred at the highest frequency (23 times), and one HMX molecule decomposed and released three NO_2 molecules. The $C_4H_8O_8N_8 \rightarrow C_4H_8O_4N_6 + 2NO_2$ reaction occurred 17 times at 0.2 ps, and one HMX molecule decomposed to release two NO_2 molecules. At 0.2 ps, the $C_4H_8O_8N_8 \rightarrow C_4H_8N_4 + 4NO_2$ reaction occurred 12 times. Combined with the result that NO_2 appeared earlier than HNO_2 in Fig. 5(b), the most likely initial reaction mechanism of nano-HMX is $N–NO_2$ bond breakage and NO_2 release.

This result indicates that the $N–NO_2$ bond is decomposed in nano-HMX. This phenomenon is consistent with the result that LEWIS used BLYP and B3LYP to explore the decomposition path of HMX in the gas phase. LEWIS found that the reaction energy barrier of $N–NO_2$ cleavage (40.5–41.8 kcal mol^{-1}) was the lowest among four possible paths (HONO elimination, C–N bond breaking, and joint ring opening); that is, $N–NO_2$ cleavage was the most likely cleavage path of HMX. The most frequent of the three reactions was the release of multiple NO_2 molecules from a nano-HMX molecule, which adequately explains the rapid growth rate of NO_2 after the initial reaction in Fig. 5. At 0.2 ps, the $C_4H_8O_8N_8 \rightarrow C_4H_7ON_5 + OH + 3NO_2$ reaction occurred twice. The appearance of OH adequately explains the phenomenon that OH appears earlier than H in Fig. 5, while the HNO_2 fragment in R3, R4, R7, and R8 adequately explains the phenomenon that the amount of OH is greater than H in Fig. 5.

One of the results reported by the software is that the net flux (NF) indicates how often the reaction is observed during the simulation time. Table 3 demonstrates the relatively higher NF of the reactions that have relatively higher NF at 2000 K and 3000 K.

One of the major intermediate species is R-N$_2$ for the maximum net flux. The important reactions that release N$_2$ occur due to the high concentration of N$_2$, and this molecule appears at (R0, 2, 5, 6, 9, 11, 13, 17, 27, 30, 33, 42, 49, 52, 54, 56, 58). Another major intermediate is R-CO$_2$ for releasing CO$_2$, and this molecule appears at (R0, 25, 60). The overall analysis of simulations shows that the other main product gas is CO$_2$. The other main intermediate is R-H$_2$O to release H$_2$O, and this molecule appears at (R38, 44, 48). The chemical effect of H$_2$O can be expressed in terms of two types of reactions: $H_2O_2N \rightarrow ON + H_2O$ (R38) and $HO + HON \rightarrow ON + H_2O$ (R44).

4. Conclusions

In this work, the decomposition mechanism of octahydro-1,3,5,7-tetranitro-1,3,5,7-tetrazocine (HMX) and nano-HMX by size effect and temperature was studied by ReaxFF-lg reactive MD. The results illustrate the detailed mechanism and

morphological evolution of HMX and its nanospheres. The main conclusions are as follows:

(1) For the variation rate in the PE curve of HMX and nano-particles with different sizes at different temperatures, it was found that the nanostructure greatly influences the PE curve. However, there is little influence of the nanosize and temperature on the PE curve.

(2) By comparing the change trend of TM in the six systems at different high temperatures, it was found that the larger the nano-size, the higher the reaction temperature, and the more intense the reaction.

(3) By analyzing the temperature distribution of nano-HMX, it was found that the heat conduction process of the entire reaction was endothermic, heat transfer, pyrolysis and heat release, and the corresponding morphological change of nanospheres was vibration-sphere dissociation and diffusion.

(4) For the variation in the main intermediate fragments and products, it was found that the nanostructure and high temperature have a strong influence on the main fragments, while there is little influence of nanosize on the pyrolysis reaction.

(5) At 3000 K, the initial decomposition reaction of 30 Å nano-HMX is $C_4H_8O_8N_8 \rightarrow C_4H_8O_2N_5 + 3NO_2$, which occurs at a maximum frequency of 23 times at 0.2 ps. The most likely initial reaction mechanism of nano-HMX is $N–NO_2$ bond breaking and NO_2 release.

We expect that these theoretical studies of the reaction of HMX might stimulate further experimental studies of nanoparticle-HMX, particularly the synthesis and characterization.

Conflicts of interest

There are no conflicts to declare.

Acknowledgements

References

1 N. N. Ge, Y. K. Wei, G. F. Ji, X. R. Chen, F. Zhao and D. Q. Wei, Initial decomposition of the condensed-phase β-HMX under shock waves: molecular dynamics simulations, *J. Phys. Chem. B*, 2012, **116**(46), 13696–13704, DOI: **10.1021/jp309120t**.

2 N. N. Ge, Y. K. Wei, Z. F. Song, X. R. Chen, G. F. Ji, F. Zhao and D. Q. Wei, Anisotropic responses and initial decomposition of condensed-phase β-HMX under shock loadings via molecular dynamics simulations in

conjunction with multiscale shock technique, *J. Phys. Chem. B*, 2014, **118**(29), 8691–8699, DOI: **10.1021/jp502432g**.

3 O. Sharia and M. M. Kuklja, Modeling thermal decomposition mechanisms in gaseous and crystalline molecular materials: application to β-HMX, *J. Phys. Chem. B*, 2011, **115**(44), 12677–12686, DOI: **10.1021/jp202733d**.

4 F. P. Bowden and A. D. Yoffe, *Fast reactions in solids*, Butterworths Scientific Publications, 1958, DOI: **10.1063/1.3060863**.

5 S. M. Walley, J. E. Field and M. W. Greenaway, Crystal sensitivities of energetic materials, *Mater. Sci. Technol.*, 2006, **22**(4), 402–413, DOI: **10.1179/174328406X91122**.

6 O. Sharia and M. M. Kuklja, Rapid materials degradation induced by surfaces and voids: ab initio modeling of β-octatetramethylene tetranitramine, *J. Am. Ceram. Soc.*, 2012, **134**(28), 11815–11820, DOI: **10.1021/ja3044695**.

7 X. H. Duan, W. P. Li, C. H. Pei and X. Q. Zhou, Molecular dynamics simulations of void defects in the energetic material HMX, *J. Mol. Model.*, 2013, **19**(9), 3893–3899, DOI: **10.1007/s00894-013-1924-7**.

8 Z. H. He, J. Chen, G. F. Ji, L. M. Liu, W. J. Zhu and Q. Wu, Dynamic responses and initial decomposition under shock loading: a DFTB calculation combined with MSST method for β-HMX with molecular vacancy, *J. Phys. Chem. B*, 2015, **119**(33), 10673–10681, DOI: **10.1021/acs.jpcb.5b05081**.

9 M. M. Kuklja, R. V. Tsyshevsky and O. Sharia, Effect of polar surfaces on decomposition of molecular materials, *J. Am. Chem. Soc.*, 2014, **136**(38), 13289–13302, DOI: **10.1021/ja506297e**.

10 M. M. Kuklja, O. Sharia and R. Tsyshevsky, Conveying chirality onto the electronic structure of achiral metals:(R,R)-tartaric acid on nickel, *Surf. Sci.*, 2004, **554**(2–3), 141–149, DOI: **10.1016/j.susc.2003.12.060**.

11 G. Liu, B. Tian, S. H. Wei and C. Zhang, Polymorph-dependent initial thermal decay mechanism of energetic materials: a case of 1, 3, 5, 7-Tetranitro-1, 3, 5, 7-Tetrazocane, *J. Phys. Chem. C*, 2021, **125**(18), 10057–10067, DOI: **10.1021/acs.jpcc.1c01056**.

12 R. W. Armstrong, Dislocation mechanics aspects of energetic material composites, *Rev. Adv. Mater. Sci.*, 2009, **19**(1/2), 13–40, DOI: **10.1016/jphyse.2008.12.005**.

13 M. M. Kuklja and A. B. Kunz, Electronic structure of molecular crystals containing edge dislocations, *J. Appl. Phys.*, 2001, **89**(9), 4962–4970, DOI: **10.1063/1.1359171**.

14 A. B. Kunz and D. R. Beck, Possible role of charged defects in molecular solids, *Phys. Rev. B: Condens. Matter Mater. Phys.*, 1987, **36**(14), 7580, DOI: **10.1103/PhysRevB.36.7580**.

15 M. M. Kuklja and S. N. Rashkeev, Molecular instability at the shear-stress interface, DYMAT-International Conference on the Mechanical and Physical Behaviour of Materials under Dynamic Loading, *EDP Sciences*, 2009, **2**, 1723–1728, DOI: **10.1051/dymat/2009243**.

16 E. J. Reed, Electron-ion coupling in shocked energetic materials, *J. Phys. Chem. C*, 2012, **116**(3), 2205–2211, DOI: **10.1021/jp206769c**.

17 (*a*) A. Bhattacharya, Y. Q. Guo and E. R. Bernstein, Experimental and theoretical exploration of the initial steps in the decomposition of a model nitramine energetic material: Dimethylnitramine, *J. Phys. Chem. A*, 2009, **113**(5), 811–823, DOI: **10.1021/jp807247t**; (*b*) A. Bhattacharya and E. R. Bernstein, Conformation specific and charge directed reactivity of radical cation intermediates of α-substituted (amino, hydroxy, and keto) bioactive carboxylic acids, *Phys. Chem. Chem. Phys.*, 2010, **12**(33), 9700–9712, DOI: **10.1021/jp109152p**.

18 M. M. Kuklja, E. V. Stefanovich and A. B. Kunz, An excitonic mechanism of detonation initiation in explosives, *J. Chem. Phys.*, 2000, **112**(7), 3417–3423, DOI: **10.1063/1.480922**.

19 M. M. Kuklja, On the initiation of chemical reactions by electronic excitations in molecular solids, *Appl. Phys. A: Mater. Sci. Process.*, 2003, **76**(3), 359–366, DOI: **10.1007/s00339-002-1821-x**.

20 E. D. Aluker, A. G. Krechetov, A. Y. Mitrofanov, D. R. Nurmukhametov and M. M. Kuklja, Laser initiation of energetic materials: selective photoinitiation regime in pentaerythritol tetranitrate, *J. Phys. Chem. C*, 2011, **115**(14), 6893–6901, DOI: **10.1021/jp1089195**.

21 A. E. van der Heijden and R. H. Bouma, Crystallization and characterization of RDX, HMX, and CL-20, *Cryst. Growth Des.*, 2004, **4**(5), 999–1007, DOI: **10.1021/cg049965a**.

22 X. Z. Yong, L. Dabin and X. L. Chun, Preparation and characterization of reticular nano-HMX[J], *Propellants, Explos., Pyrotech.*, 2005, **30**(6), 438–441, DOI: **10.1002/prep.200500038**.

23 M. A. Barreto-Cabán, L. Pacheco-Londoño, M. L. Ramírez and S. P. Hernández-Rivera, Novel method for the preparation of explosive nanoparticles, Sensors, and Command, Control, Communications, and Intelligence (C3I) Technologies for Homeland Security and Homeland Defense V, *SPIE*, 2006, **6201**, 644–654, DOI: **10.1117/12.666147**.

24 A. E. D. M. van der Heijden, Y. L. M. Creyghton and E. Marino, Energetic materials: crystallization, characterization and insensitive plastic bonded explosives, *Propellants, Explos., Pyrotech.*, 2008, **33**(1), 25–32, DOI: **10.1002/prep.200800204**.

25 D. Spitzer, M. Comet, C. Baras, V. Pichot and N. Piazzon, Energetic nano-materials: Opportunities for enhanced performances, *J. Phys. Chem. Solids*, 2010, **71**(2), 100–108, DOI: **10.1016/j.jpcs.2009.09.010**.

26 N. Radacsi, A. I. Stankiewicz, Y. L. Creyghton, A. E. van der Heijden and J. H. ter Hor, Electrospray crystallization for high-quality submicron-sized crystals, *Chem. Eng. Technol.*, 2011, **34**(4), 624–630, DOI: **10.1002/ceat.201000538**.

27 B. Risse, D. Spitzer, D. Hassler, F. Schnell, M. Comet, V. Pichot and H. Muhr, Continuous formation of submicron energetic particles by the flash-evaporation technique, *Chem. Eng. J.*, 2012, **203**, 158–165, DOI: **10.1016/j.cej.2012.07.032**.

28 N. Radacsi, A. E. D. M. van der Heijden, A. I. Stankiewicz and J. H. Ter Horst, Cold plasma synthesis of high quality organic nanoparticles at atmospheric pressure, *J. Nanopart. Res.*, 2013, **15**(2), 1–13, DOI: **10.1007/s11051-013-1445-4**.

29 B. Wang, X. Liao, Z. Wang, L. T. DeLuca, Z. Liu and W. He, Effects of particle size and morphology of NQ on thermal and combustion properties of triple-base propellants, *Combust. Flame*, 2018, **193**, 123–132, DOI: **10.1016/j.combustflame.2018.03.009**.

30 G. Li, L. Niu, W. Hao, Y. Liu and C. Zhang, Atomistic insight into the microexplosion-accelerated oxidation process of molten aluminum nanoparticles, *Combust. Flame*, 2020, **214**, 238–250, DOI: **10.1016/j.combustflame.2019.12.027**.

31 X. Zhang, C. Fu, Y. Xia, Y. Duan, Y. Li, Z. Wang and H. Li, Atomistic origin of the complex morphological evolution of aluminum nanoparticles during oxidation: a chain-like oxide nucleation and growth mechanism, *ACS Nano*, 2019, **13**(3), 3005–3014, DOI: **10.1021/acsnano.8b07633**.

32 J. Y. Lyu, J. H. Yu, D. Y. Tang, W. He, B. W. Tao, X. Guo and Q. L. Yan, Unexpected burning rate independence of composite propellants on the pressure by fine interfacial control of fuel/oxidizer, *Chem. Eng. J.*, 2020, **388**, 124320, DOI: **10.1016/j.cej.2020.124320**.

33 J. H. Yi, F. Q. Zhao, W. L. Hong, S. Y. Xu, R. Z. Hu, Z. Q. Chen and L. Y. Zhang, Effects of Bi-NTO complex on thermal behaviors, nonisothermal reaction kinetics and burning rates of NG/TEGDN/NC propellant, *J. Hazard. Mater.*, 2010, **176**(1–3), 257–261, DOI: **10.1016/j.jhazmat.2009.11.021**.

34 C. An, S. Xu, Y. Zhang, B. Ye, X. Geng and J. Wang, Nano-HNS particles: mechanochemical preparation and properties investigation, *J. Nanomater.*, 2018, **2018**, 1–7, DOI: **10.1155/2018/9436089**.

35 X. Guo, J. Wang, J. Ran, L. Zhao, Y. Han and W. Cao, Shock initiation of nano-TATB explosives under short-duration pulses, *Propellants, Explos., Pyrotech.*, 2019, **44**(2), 138–143, DOI: **10.1002/prep.201800260**.

36 J. Liu, W. Jiang, Q. Yang, J. Song, G. Z. Hao and F. S. Li, Study of nano-nitramine explosives: preparation, sensitivity and application, *Def. Technol.*, 2014, **10**(2), 184–189, DOI: **10.1016/j.dt.2014.04.002**.

37 X. Jia, J. Wang, C. Hou and Y. Tan, Green preparation, spheroidal, and superior property of nano-1, 3, 5, 7-tetranittro-1, 3, 5, 7-tetrazocane, *J. Nanomater.*, 2018, **2018**, 5839037, DOI: **10.1155/2018/5839037**.

38 Z. Liu, W. Zhu, G. Ji, K. Song and H. Xiao, Decomposition mechanisms of α-octahydro-1, 3, 5, 7-tetranitro-1, 3, 5, 7-tetrazocine nanoparticles at high temperatures, *J. Phys. Chem. C*, 2017, **121**(14), 7728–7740, DOI: **10.1021/acs.jpcc.7b01136**.

39 S. Zhu and W. Zhu, Simplified predictions of Hamaker constants from Lifshitz theory, *J. Nanopart. Res.*, 2021, **125**(1), 1–13, DOI: **10.1007/s11051-020-05099-9**.

40 S. Plimpton, Fast parallel algorithms for short-range molecular dynamics, *J. Comput. Phys.*, 1995, **117**(1), 1–19, DOI: **10.1006/jcph.1995.1039**.

41 D. Furman, R. Kosloff, F. Dubnikova, S. V. Zybin, W. A. Goddard III, N. Rom and Y. Zeiri, Decomposition of condensed phase energetic materials: interplay between uni-and bimolecular mechanisms, *J. Am. Chem. Soc.*, 2014, **136**(11), 4192–4200, DOI: **10.1021/ja410020f**.

42 L. Chen, H. Wang, F. Wang, D. Geng, J. Wu and J. Lu, Thermal decomposition mechanism of 2, 2′, 4, 4′, 6, 6′-hexanitrostilbene by reaxFF reactive molecular dynamics simulations, *J. Phys. Chem. C*, 2018, **122**(34), 19309–19318, DOI: **10.1021/acs.jpcc.8b03463**.

43 Y. Xiao, L. Chen, K. Yang, D. Geng, J. Lu and J. Wu, Mechanism of the improvement of the energy of host–guest explosives by incorporation of small guest molecules: HNO$_3$ and H$_2$O$_2$ promoted C–N bond cleavage of the ring of ICM-102, *Sci. Rep.*, 2021, **11**(1), 1–12, DOI: **10.21203/rs.3.rs-294160/v1**.

44 Q. Lan, H. Zhang, Y. Ni, J. Chen and H. Wang, Thermal decomposition mechanisms of LLM-105/HTPB plastic-bonded explosive: reaxFF-lg molecular dynamics simulations, *J. Energ. Mater.*, 2021, 1–22, DOI: **10.1080/07370652.2021.1968071**.

45 Z. Mei, Q. An, F. Q. Zhao, S. Y. Xu and X. H. Ju, Reactive molecular dynamics simulation of thermal decomposition for nano-aluminized explosives, *Phys. Chem. Chem. Phys.*, 2018, **20**(46), 29341–29350, DOI: **10.1039/c8cp05006f**.

46 L. Song, F. Q. Zhao, S. Y. Xu, C. C. Ye and X. H. Ju, Structural evolution of aluminum hydride nanoparticles in water using reaxFF molecular dynamics method, *Mater. Today Commun.*, 2021, **26**, 101804, DOI: **10.1016/j.mtcomm.2020.101804**.

47 D. Xiang, X. Xie and P. Yao, Atomistic insight into thermal decomposition of 1, 3, 5-triamino-2, 4, 6-trinitrobenzene nanoparticles according to the reaxFF molecular dynamics method, *ChemistrySelect*, 2022, **7**(2), e202102465, DOI: **10.1002/slct.202102465**.

48 M. R. Manaa, E. J. Reed, L. E. Fried and N. Goldman, Nitrogen-rich heterocycles as reactivity retardants in shocked insensitive explosives, *J. Am. Chem. Soc.*, 2009, **131**(15), 5483–5487, DOI: **10.1021/ja808196e**.

49 M. R. Manaa, L. E. Fried, C. F. Melius, M. Elstner and T. Frauenheim, Nitrogen-rich heterocycles as reactivity retardants in shocked insensitive explosives, *J. Phys. Chem. A*, 2002, **106**(39), 9024–9029, DOI: **10.1021/jp025668+**.

50 R. H. Byrd, P. Lu, J. Nocedal and C. Zhu, A limited memory algorithm for bound constrained optimisation, *SIAM J. Sci. Comput.*, 1995, **16**(5), 1190–1208, DOI: **10.1137/0916069**.

51 M. A. Wood, A. C. Van Duin and A. Strachan, Coupled thermal and electromagnetic induced decomposition in the molecular explosive αHMX; a reactive molecular dynamics study, *J. Phys. Chem. A*, 2014, **118**(5), 885–895, DOI: **10.1021/jp406248m**.

52 C. J. Wu, L. E. Fried, L. H. Yang, N. Goldman and S. Bastea, Catalytic behaviour of dense hot water, *Nat. Chem.*, 2009, **1**(1), 57–62, DOI: **10.1038/nchem.130**.

53 F. Guo, X. L. Cheng and H. R. Zhang, Reactive molecular dynamics simulation of solid nitromethane impact on (010) surfaces induced and nonimpact thermal decomposition, *J. Phys. Chem.*, 2012, **116**(14), 3514–3520, DOI: **10.1021/jp211914e**.

54 A. Strachan, A. C. van Duin, D. Chakraborty, S. Dasgupta and W. A. Goddard III, Shock waves in high-energy materials: the initial chemical events in nitramine RDX, *Phys. Rev. Lett.*, 2003, **91**(9), 098301, DOI: **10.1103/PhysRevLett.91.098301**.